Holographic Microscopy for 3D Tracking of Bacteria

Jay Nadeau[1,2], Yong Bin Cho[1], Marwan El-Kholy[2], Manuel Bedrossian[1], Stephanie Rider[1], Christian Lindensmith[3], J. Kent Wallace[3]

[1]GALCIT, California Institute of Technology 1200 E. California Blvd. Pasadena, CA 91125. USA
[2] Department of Biomedical Engineering, McGill University, Montreal, QC H3A 2B4 Canada
[3]Jet Propulsion Laboratory, California Institute of Technology, 4800 Oak Grove Dr. Pasadena, CA 91109. USA

ABSTRACT

Understanding when, how, and if bacteria swim is key to understanding critical ecological and biological processes, from carbon cycling to infection. Imaging motility by traditional light microscopy is limited by focus depth, requiring cells to be constrained in *z*. Holographic microscopy offers an instantaneous 3D snapshot of a large sample volume, and is therefore ideal in principle for quantifying unconstrained bacterial motility. However, resolving and tracking individual cells is difficult due to the low amplitude and phase contrast of the cells; the index of refraction of typical bacteria differs from that of water only at the second decimal place. In this work we present a combination of optical and sample-handling approaches to facilitating bacterial tracking by holographic phase imaging. The first is the design of the microscope, which is an off-axis design with the optics along a common path, which minimizes alignment issues while providing all of the advantages of off-axis holography. Second, we use anti-reflective coated etalon glass in the design of sample chambers, which reduce internal reflections. Improvement seen with the antireflective coating is seen primarily in phase imaging, and its quantification is presented here. Finally, dyes may be used to increase phase contrast according to the Kramers-Kronig relations. Results using three test strains are presented, illustrating the different types of bacterial motility characterized by an enteric organism (*Escherichia coli*), an environmental organism (*Bacillus subtilis*), and a marine organism (*Vibrio alginolyticus*). Data processing steps to increase the quality of the phase images and facilitate tracking are also discussed.

Keywords:

Holography, Microscopy, Motility, tracking, Digital Holographic Microscopy (DHM), Quantitative Phase Imaging (QPI), Phase Contrast, Kramers-Kronig Relations

1. INTRODUCTION

Digital holographic microscopy (DHM) is a technique of interferometric microscopy. In the off-axis configuration, an object beam interacts with a sample, then combines with a reference beam to encode both the amplitude and phase of the light as an interference pattern. This pattern is a hologram, and can be used to numerically reconstruct the object beam at any location in the sample volume[1-3] [4]. The main advantage of DHM over light microscopy is that it is able to capture a complete three-dimensional sample volume (usually hundreds of micrometers thick) simultaneously, so that manual focusing during data acquisition is not needed. This makes DHM ideal for field situations and autonomous deployment. The advantage of off-axis over in-line DHM is that the former permits independent reconstruction of both amplitude and phase. Amplitude images correspond to brightfield light microscopy, and thus are often low in contrast for biological specimens such as cells, which tend to be pure phase objects. Contrast in phase images $\Delta\varphi$ is proportional to the difference in indices of refraction between the medium (n_m) and cell (n_c)[5]:

$$\Delta\varphi = \frac{2\pi}{\lambda} h(x,y)[n_c(x,y) - n_m] \quad (1)$$

Where λ is the wavelength of illumination and h is the thickness of the object at the measured point; n_c represents a z-integrated value at that same point and thus also depends upon the nature of the sample.

Changes in cell index of refraction occur when the ratio of water to solutes changes due to any of a large number of physiological and pathological processes. Quantitative phase imaging has been used to monitor programmed cell death

Quantitative Phase Imaging II, edited by Gabriel Popescu, YongKeun Park, Proc. of SPIE Vol. 9718, 97182B

(apoptosis), to distinguish cancer cells from healthy cells, and to observe changes in cell volume that occur when solution osmolarity is changed. [6] [7] [8] [9] [10] [11]. Studies have reported sensitivities as high as 4 x 10^{-4} in refractive index [5]. However, such experiments are very challenging, requiring noise-reduction techniques and background phase monitoring.

Compared with eukaryotic cells, non-photosynthetic bacteria show substantially less amplitude and phase contrast. Brightfield microscopic techniques for bacterial imaging have relied upon dyes and stains since the days of Ehrlich and Koch, since the unlabelled cells are essentially invisible. Differential interference contrast (DIC) and Zernicke phase contrast may also be used to image bacterial cells. The use of DHM for bacterial imaging is in its infancy, due to three primary factors: lack of spatial resolution of most instruments, lack of contrast of the samples, and system noise interfering with bacterial detection.

Sources of noise include vibrations, laser speckle, and *temporal phase noise* resulting from uncorrelated noise between the two fields of the interferometer. Both pre and post-processing filtering methods are used to reduce noise. The setup may be optimized by reducing the recording distance and using a CCD camera with a smaller pixel size[12]. Other methods to reduce noise include phase error compensation, spatial light modulation (SLM), and multiple frequency overlapping[13-16], which improve the reconstructed phase image of holograms. Noise reduction is also accomplished by filtering certain frequencies, both in the spatial and Fourier planes, with Butterworth filters and masks, respectively[17-19]. In addition, efficient encoding methods and correlation based de-noising algorithms have been developed to significantly reduce speckle noise[20, 21]. During biological studies, the power of the light source must be monitored as to not harm the organisms being observed. This has prompted investigation into the reduction of errors introduced by shot noise, as well as irregularities in photonic activity that become dominant when photonic density decreases[22, 23].

A significant source of noise in the phase-shift reconstruction of holographic images arises from the substrate used to contain the sample being investigated. Polydimethylsiloxane (PDMS) and other polymer based microfluidic channels are often used to contain cells for light microscopy, due to PDMS's low effect on light intensity imaging[24, 25]. PDMS channels have also been reported for DHM, though no phase imaging was performed[26].

Several papers on the use of DHM for bacterial tracking have recently appeared. One paper reported a de-noising algorithm for the identification of bacteria from in-line holograms[27]. Such techniques come at a great computational cost. Another paper reported the use of amplitude times the square of the phase as a contrast-enhancement technique for off-axis holography. We have recently reported the use of a corrole dye to enhance phase contrast in bacterial DHM imaging [28]. Dyes increase phase contrast when the wavelength of illumination is longer than that of the dye's absorbance peak according to the Kramers-Kronig relations, which give a formula for the change in refractive index as a function of wavelength:

$$\Delta n(\lambda) = \frac{-2\lambda^2}{\pi} \mathcal{P} \int_{\delta}^{\infty} \frac{n_{img}(\lambda')}{\lambda'(\lambda'^2 - \lambda^2)} d\lambda' \qquad (2),$$

where $\mathcal{P}$ is the Cauchy principal value and the value δ is included to avoid divergence at $\lambda = 0$. For illumination at 405 nm, a corrole dye—which has a strong Soret absorption band in the violet to blue—was an ideal choice. Corroles (and porphyrins) also show very strong absorbance, up to 10^5 $M^{-1}cm^{-1}$ at the Soret peak.

In this paper we illustrate how instrument design, sample chamber refinement, and the use of dyes may all be used to facilitate 3D bacterial detection using off-axis DHM phase imaging. Results for three strains are presented, illustrating the reduced noise obtainable in phase vs. amplitude images and the ability to apply automated thresholding to selected samples. These results should be useful to all users of off-axis DHM, both to inform instrument design and for use with existing instruments.

2. INSTRUMENT DEVELOPMENT

The nature of holography causes holographic imaging instruments to be highly sensitive to physical vibrations and alignment issues. To address this, an off-axis digital holographic microscope was developed with a common light source

for both reference and specimen beams that share an identical optical path. This attenuates any sensitivities to vibration and alignment as the two beams of light travel through a single common-mode.

2.1 Instrument Description

A diagram of the optical system is shown in **Figure 1(a)**. This diagram captures the key components but is not to scale, so lengths and angles are not representative of the as-built system, as shown in the CAD drawing in **Figure 1(b)**. The specifications of the design are tabulated in Table 1.

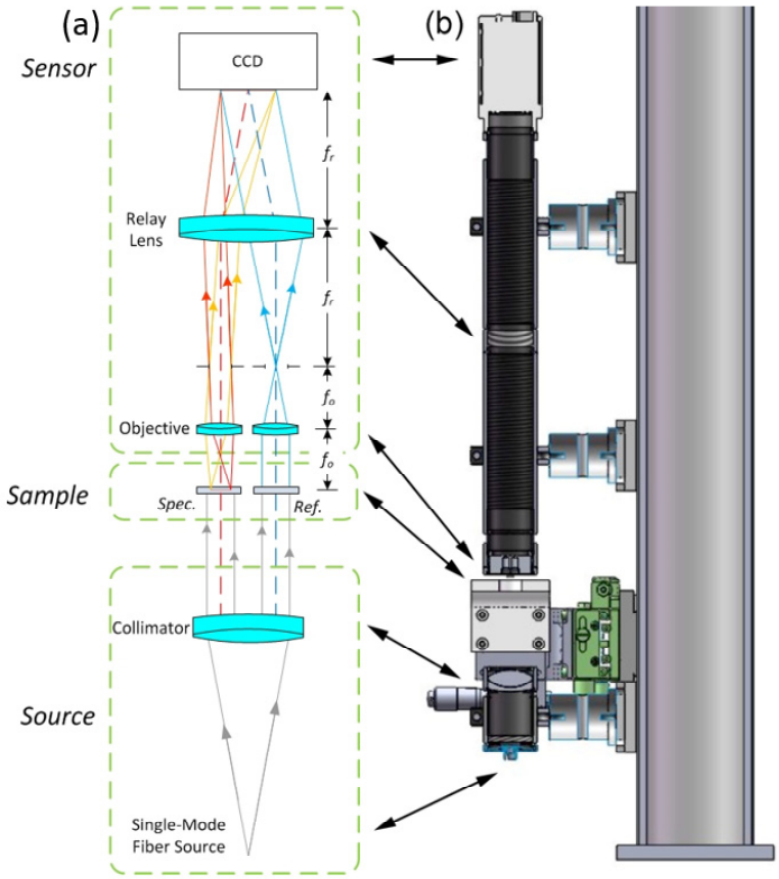

Figure 1. Schematic and images of the compact, twin-beam digital holographic microscope in its laboratory implementation. (a) Schematic showing four main elements: the source, the sample (specimen path is labelled Spec. and reference path is labelled Ref.), the microscope, and the sensor. (b) Solid model of the hardware. The fiber-fed source assembly is at the bottom, and the imaging camera is at the top. The microscope optics – comprised of the two aspheric lenses and the relay lens – are contained within the 300 mm long lens tube. The three- axis stage between the source the microscope optics provides easy manual manipulation of the specimen under study[29].

2.2 Instrument Performance

This compact, twin beam off-axis DHM instrument provides robust, diffraction limited performance. With validated sub-micron lateral-resolution, and a depth of focus on the order of hundreds of microns, this device is able to image large volumes at a time, without any sacrifice in performance.

The robustness and insensitivity to alignment and vibration were tested during a field deployment to Nuuk, Greenland in March of 2015. During deployment, this optical design was integrated into an ‘all-in-one’ instrument that included a processor, hard drive, light source, as well as other diagnostic measuring devices such as temperature and moisture sensors.

Table 1: Fundamental Properties of the compact, twin-beam DHM system[29]

Property	*Value*	*Unit*	*Note*
Operating Wavelength	405	nm	Single-mode fiber-couple laser
Objective focal length - f_o	7.6	mm	Aspheric singlet
Objective Numerical Aperture	0.30	-	-
Relay lens focal length - f_r	150	mm	Achromatic doublet
System magnification	19.7	-	-
Lateral resolution	0.7	μm	-
CCD pixel size	3.45 x 3.45	μm x μm	2448 x 2050 CCD chip
Sample imaging volume	360 x 360 x >600*	μm x μm x μm	In 2048 x 2048 (4Mpx) mode
Sampling rate	15	frames per sec	4Mpx mode; 22 fps with 1Mpx
Instrument length	400	mm	Input fiber to back of CCD

**A measurement of the instrument lateral resolution for different depths demonstrated it is capable of < 1 μm lateral resolution over a sample depth of 900 μm. Our sample chamber is 600 μm deep.*

3. SAMPLE CHAMBER REFINEMENT

In order to facilitate feasible 3D detection and tracking of bacteria, it is desirable to eliminate as much noise as possible before data are collected. This reduces the necessity to computationally de-noise images after the fact. Through the refinement of the optical quality of sample chambers used in DHM, the intrinsic noise of a twin-beam off-axis DHM instrument was reduced, while increasing the Signal to Noise Ratio (SNR), using anti-reflective (AR) coated etalon glass.

A total of six sample chamber configurations were tested by measuring their background noise and SNR values. These six sample chamber configurations varied the type of substrate in the optical path of the instrument. These six configurations consisted of: 1) A sample chamber with etalon glass on both sides of the chamber with an AR coating at 405 nm, 2) a sample chamber with non-AR coated etalon glass in the optical path, 3) a sample chamber with conventional microscope slide glass in the optical path, 4) a sample chamber with a combination of conventional microscope slide glass and non-AR coated etalon glass in the optical path, 5) a commercially available polycarbonate sample chamber from Electron Microscopy Sciences, and 6) a custom made polydimethylsiloxane (PDMS) microchannel.

Background noise was measured by the analysis of empty sample chambers. The local and global standard deviations of the images obtained from these empty chambers were quantified. **Figure 2** shows the average background noise values of the various sample chamber configurations.

Both the AR and non-AR coated etalon sample chambers significantly reduced the amount of background noise of numerically reconstructed phase images compared to that of conventional microscope slide sample chambers. AR and non-AR coated sample chambers provided similar amounts of background noise, although the AR coated etalons performed much more consistently than their non-AR coated counterparts. Both AR and non-AR coated etalon sample chambers reduced background noise by 12.7%, compared to sample chambers consisting of conventional microscope slide glass.

The SNR is a ratio that is defined as the amplitude of a signal of interest divided by its neighboring noise. We define the amplitude of the signal as:

$$S = P_I - \overline{N_b} \tag{3}$$

Where S is the signal value, P_I is the peak intensity, and $\overline{N_b}$ is the average background noise. Noise is defined as:

$$N = \sigma_{noise} \tag{4}$$

Where N is the noise value, and σ_{noise} is the standard deviation of the background greyscale values neighboring the signal. Combining these two definitions, the SNR becomes:

$$\mathrm{SNR} = \frac{S}{N} \tag{5}$$

Using *Bacillus subtilis* as the signal, hundreds of SNR calculations were made per sample chamber configuration. Figure 3 show the mean SNR values of the different sample chamber configurations.

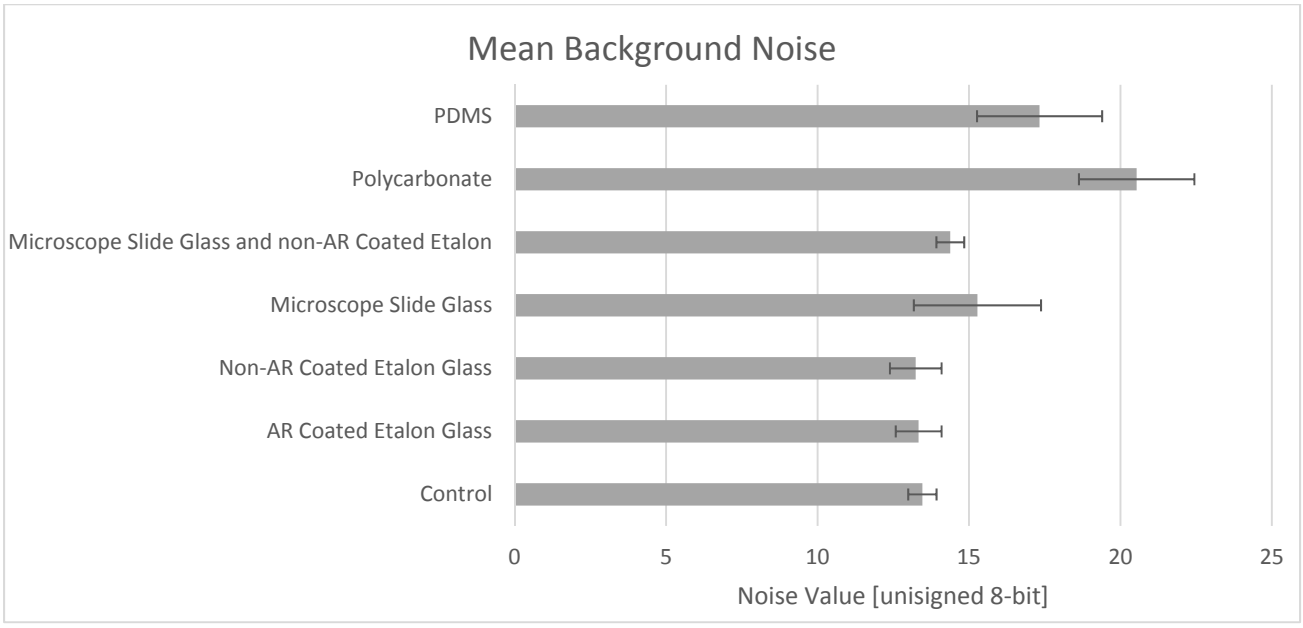

Figure 2. Mean noise values of different sample chambers compared to "Control" reference

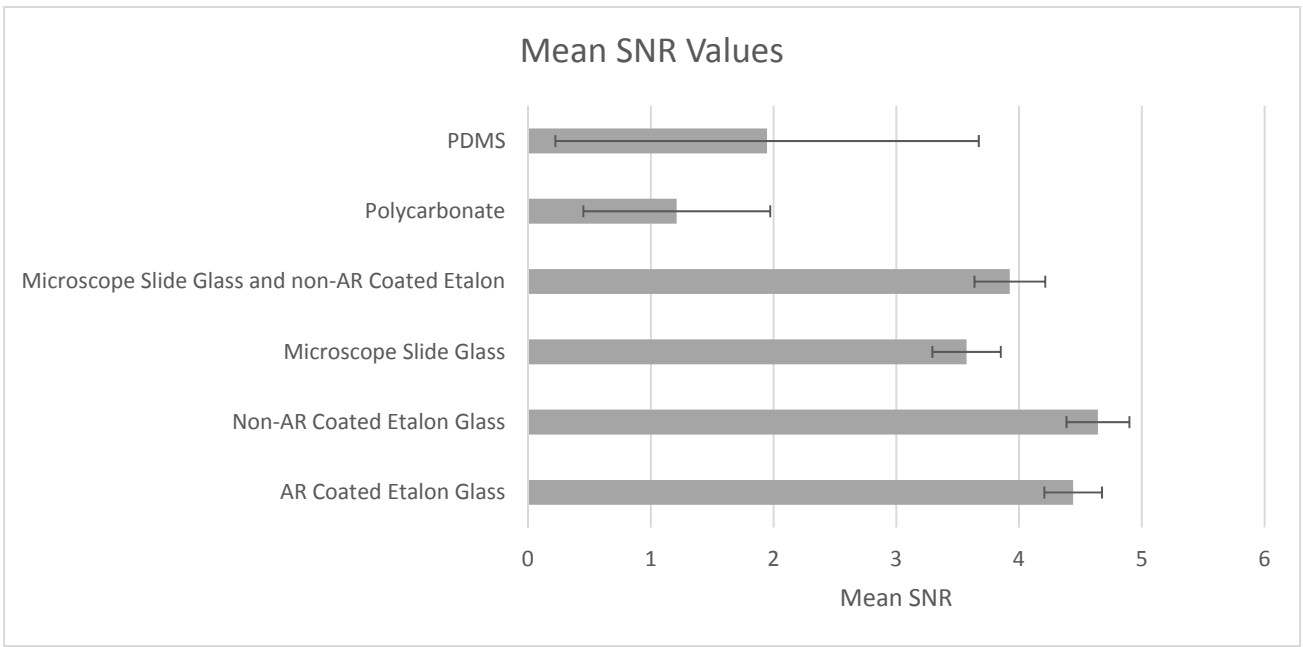

Figure 3. Mean and standard deviation of SNR values for each sample chamber configuration (polycarbonate chamber labeled as 'Polymer')

4. BACTERIAL TEST STRAINS WITH AND WITHOUT DYES

Test strains were purchased from the American Type Culture Collection (ATCC): *Bacillus subtilis*, *Escherichia coli*, and *Vibrio alginolyticus*. *B. subtilis* and *E. coli* were maintained on lysogeny broth and *V. alginolyticus* on 2216 marine broth. Imaging was performed in minimal "motility medium" consisting of 10 mM potassium phosphate, 10 mM NaCl, 0.1 mM EDTA, 0.1 mM glucose, pH 7.0. Tracking was performed using Fiji [30]. When dye was used, it was added at a concentration of 0.2-4 μM approximately 60 min before imaging, then washed out three times by centrifugation and resuspension. The dye used was the metallocorrole, $Ga(tpfc)(SO_3H)_2$ as we have reported previously. It is a sulfonic acid-substituted dye that binds tightly to proteins; it also has a strong Soret band absorbance (~400 nm), which makes it ideal from that standpoint of Eq. (2).

Figure 4 shows phase images of the three bacterial test strains with and without dye. Some increase in amplitude contrast was seen with this dye (not shown), but its primary effect was on phase. Increased phase contrast may be appreciated not only as an increased visibility of cells at best focus, but an increased visibility of each cell across multiple focal planes. Samples at the same density appear more crowded in the dyed case, as each cell is visible through a greater depth, and more Airy rings can be seen at each z slice.

Fig. 4 A shows unlabeled *E. coli* and **Fig. 4 B** is an *E. coli* culture with 4 μM dye. Two particular features are of note: the first is that both dyed and undyed cells could appear bright or dark depending upon the exact z-position of the phase reconstruction. As the cell passed through focus, it would switch from light to dark. This is a result of the Gouy phase anomaly[31, 32], which has been discussed in the context of DHM[33]. The magnitude of the shift was greater in dyed cells than undyed cells. Secondly, the elongated shape of many bacteria meant that cells viewed end-on looked very different than cells viewed lengthwise, due to the *h* term in Fig. (1). In controls, lengthwise cells were nearly invisible in phase images; cells lengthwise could be readily distinguished from the background. While the effect was also present in dyed cells, the biggest difference in dyed cells was that the lengthwise bacteria were readily apparent.

Fig. 4 C-F shows *B. subtilis*. These bacteria were large enough that cell structures could be seen with phase imaging, especially in the dye-labeled cells. Fig. 4 C is an unlabeled B. subtilis cell at best focus, and Fig. 4 D is the same cell ~6 μm out of focus. Fig. 4 E,F shows the same defocusing applied to a dye-labeled cell. It can be appreciated that dye labeling permits visualization of the outer perimeter of these cells.

Fig. G-J show *V. alginolyticus*, the smallest of the test strains. Increased phase contrast over undyed cells (**Fig. 4 G**) can be seen in the dyed sampled (**Fig. 4 H**). **Fig 4 I** shows a zoom-in on unlabeled cells; the increased visibility of Airy rings can be readily appreciated in **Fig. 4 J**, the labeled sample.

Most automated tracking algorithms fail to detect cells in holographic images due to the low contrast of the cells and the presence of multiple Airy rings, which are detected as objects. However, the dyed cells made the use of thresholding possible in some cases. Fig. 5 shows tracking and analysis results for *E. coli*, values consistent with the literature.

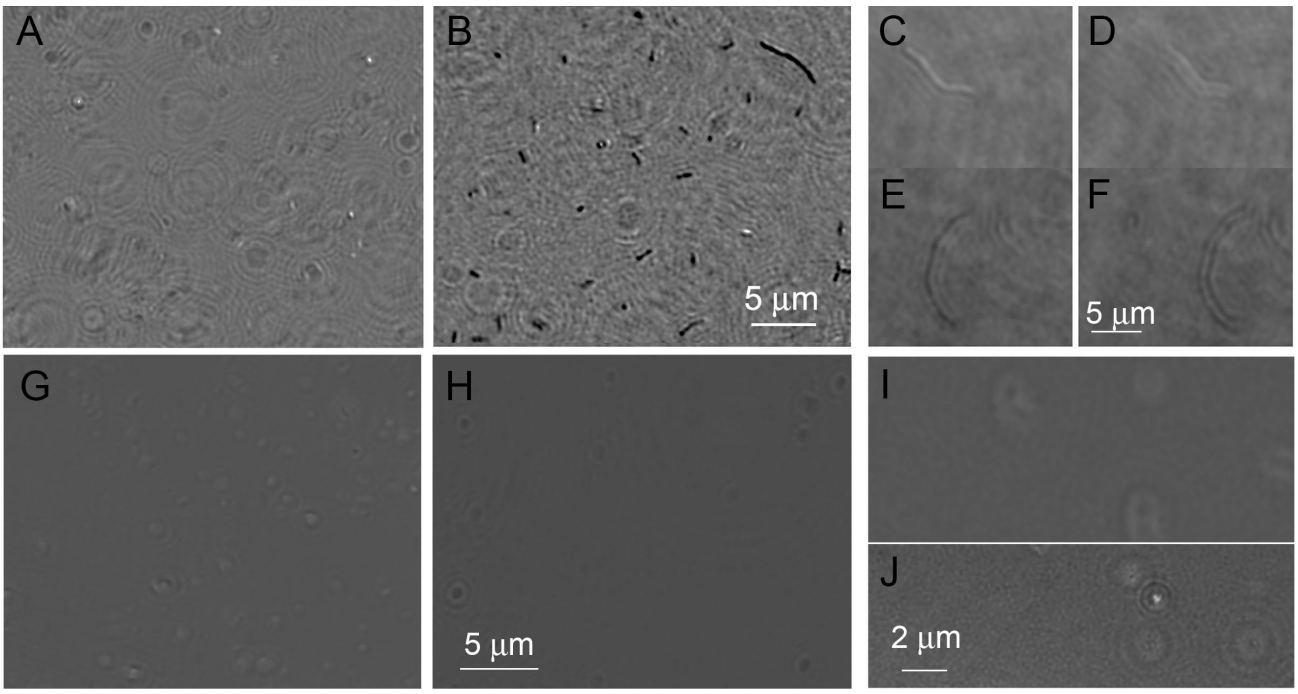

Figure 4. Single-plane phase reconstructions of bacterial cultures with and without corrole dye. (A) *E. coli* unstained. (B) *E. coli* with dye. (C) *B. subtilis* unstained at apparent best focus. (D) *B. subtilis* unstained 6 µm from best focus. (E) *B. subtilis* stained at apparent best focus. (E) *B. subtilis* stained 6 µm from best focus. (G) *V. alginolyticus* unstained. (H) V. alginolyticus stained. (I) Zoom in of *V. alginolyticus* unstained. (J) Zoom in of *V. alginolyticus* stained.

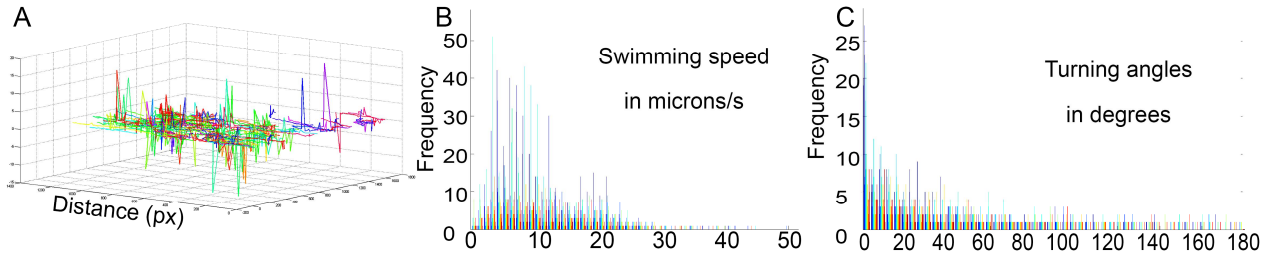

Figure 5. Analysis of *E. coli* trajectories using an automated tracking algorithm. (A) Distance travelled in x, y, and z for all of the cells identified in a given field of view. (B) Swimming speed of identified cells. (C) Turning angles.

5. DISCUSSION AND CONCLUSION

Tracking bacteria with DHM is challenging due to low contrast, small cell size, and rapid swimming with extremely fast reversals of direction. Methods such as the use of high-index media for immersion affect the vitality and hydrodynamics of the cells, making them undesirable for tracking. Here we used a combination of improved optical design, custom chambers, and dye labelling with a non-toxic agent in order to enable automated detection and tracking of bacterial test strains.

The SNR calculations showed that etalon sample chambers significantly outperformed other sample chamber configurations. Non-AR coated etalon sample chambers had a higher average SNR but was not significantly different that AR-coated etalons. In addition, AR-coated etalons performed much more reliably in terms of a smaller standard

deviation in SNR values than all other sample chamber configurations. The AR coated etalons increased the average SNR by 24% compared to that of conventional microscope slides. The combination of reduced noise and increased SNR shows the desirability of high optical quality sample chambers in the use of 3D bacterial detection and tracking.

The use of corrole or porphyrin dyes with strong absorbance in the blue is ideal for 488 nm illumination wavelengths. For more typical wavelengths used in biological experiments, other dyes may be used. For example, for 532 nm illumination, green fluorescent protein (BFP) or Syto 9 might be viable choices. It is not yet known whether these dyes are absorptive enough to be useful. The dye fluorescence is unnecessary for this application, and so colorimetric agents which absorb but do not fluoresce could also be explored.

REFERENCES

[1] P. Ferraro, S. De Nicola, A. Finizio *et al.*, "Compensation of the inherent wave front curvature in digital holographic coherent microscopy for quantitative phase-contrast imaging," Appl Opt, 42(11), 1938-46 (2003).

[2] F. Dubois, M. L. Requena, C. Minetti *et al.*, "Partial spatial coherence effects in digital holographic microscopy with a laser source," Appl Opt, 43(5), 1131-9 (2004).

[3] P. Marquet, B. Rappaz, P. J. Magistretti *et al.*, "Digital holographic microscopy: a noninvasive contrast imaging technique allowing quantitative visualization of living cells with subwavelength axial accuracy," Opt Lett, 30(5), 468-70 (2005).

[4] S. De Nicola, A. Finizio, G. Pierattini *et al.*, "Recovering correct phase information in multiwavelength digital holographic microscopy by compensation for chromatic aberrations," Opt Lett, 30(20), 2706-8 (2005).

[5] B. Rappaz, P. Marquet, E. Cuche *et al.*, "Measurement of the integral refractive index and dynamic cell morphometry of living cells with digital holographic microscopy," Opt Express, 13(23), 9361-73 (2005).

[6] F. Dubois, C. Yourassowsky, O. Monnom *et al.*, "Digital holographic microscopy for the three-dimensional dynamic analysis of in vitro cancer cell migration," J Biomed Opt, 11(5), 054032 (2006).

[7] M. Falck Miniotis, A. Mukwaya, and A. Gjorloff Wingren, "Digital holographic microscopy for non-invasive monitoring of cell cycle arrest in L929 cells," PLoS One, 9(9), e106546 (2014).

[8] P. Jourdain, N. Pavillon, C. Moratal *et al.*, "Determination of transmembrane water fluxes in neurons elicited by glutamate ionotropic receptors and by the cotransporters KCC2 and NKCC1: a digital holographic microscopy study," J Neurosci, 31(33), 11846-54 (2011).

[9] B. Kemper, D. Carl, J. Schnekenburger *et al.*, "Investigation of living pancreas tumor cells by digital holographic microscopy," J Biomed Opt, 11(3), 34005 (2006).

[10] N. Pavillon, J. Kuhn, C. Moratal *et al.*, "Early cell death detection with digital holographic microscopy," PLoS One, 7(1), e30912 (2012).

[11] B. Rappaz, B. Breton, E. Shaffer *et al.*, "Digital holographic microscopy: a quantitative label-free microscopy technique for phenotypic screening," Comb Chem High Throughput Screen, 17(1), 80-8 (2014).

[12] H. Wang, M. Yu, Y. Jiang *et al.*, "Point spread function and lateral resolution analysis of digital holographic microscopy system," Optics Communications, 322, 90-96 (2014).

[13] Z. Wang, W. Qu, Y. Wen *et al.*, "A New Phase Error Compensation Method in Digital Holographic Microscopy," International Conference on Experimental Mechanics 2014, 9302, (2015).

[14] F. Pan, W. Xiao, S. Liu *et al.*, "Coherent noise reduction in digital holographic phase contrast microscopy by slightly shifting object," Optics Express, 19(5), 3862-3869 (2011).

[15] B. Le Thanh, M. Piao, J.-R. Jeong *et al.*, "Improving Phase Contrast of Digital Holographic Microscope using Spatial Light Modulator," Journal of the Optical Society of Korea, 19(1), 22-28 (2015).

[16] X. J. Lai Xin-Ji, H.-Y. Tu, C.-H. Wu *et al.*, "Resolution enhancement of spectrum normalization in synthetic aperture digital holographic microscopy," Applied Optics, 54(1), 51-8 (2015).

[17] M. Matrecano, P. Memmolo, L. Miccio *et al.*, "Improving holographic reconstruction by automatic Butterworth filtering for microelectromechanical systems characterization," Applied Optics, 54(11), 3428-3432 (2015).

[18] A. Sharma, G. Sheoran, and Z. Jaffery, "Improvement of signal-to-noise ratio in digital holography using wavelet transform," Optics and lasers in engineering, 46(1), 42-47 (2008).

[19] E. Cuche, P. Marquet, and C. Depeursinge, "Spatial filtering for zero-order and twin-image elimination in digital off-axis holography," Applied Optics, 39(23), 4070-4075 (2000).

[20] P. Memmolo, V. Bianco, M. Paturzo *et al.*, "Encoding multiple holograms for speckle-noise reduction in optical display " Optics Express, 22(21), 25768-25775 (2014).

[21] M. Molaei Mehdi, and J. Sheng, "Imaging bacterial 3D motion using digital in-line holographic microscopy and correlation-based de-noising algorithm," Optics Express, 22(26), 32119-37 (2014).
[22] F. Charrière, T. Colomb, F. Montfort *et al.*, "Shot-noise influence on the reconstructed phase image signal-to-noise ratio in digital holographic microscopy," Applied Optics, 45(29), 7667-7673 (2006).
[23] N. Demoli, H. Skenderovic, and M. Stipcevic, "Digital holography at light levels below noise using a photon-counting approach," Optics Letters, 39(17), 5010-5013 (2014).
[24] T. Ahmed, T. S. Shimizu, and R. Stocker, "Bacterial chemotaxis in linear and nonlinear steady microfluidic gradients," Nano letters, 10(9), 3379-3385 (2010).
[25] C. Giuffre, P. Hinow, R. Vogel *et al.*, "The ciliate Paramecium shows higher motility in non-uniform chemical landscapes," PloS one, 6(4), (2011).
[26] M. Molaei, M. Barry, R. Stocker *et al.*, "Failed escape: Solid surfaces prevent tumbling of escherichia coli," Physical review letters, 113(6), 068103 (2014).
[27] M. Molaei, and J. Sheng, "Imaging bacterial 3D motion using digital in-line holographic microscopy and correlation-based de-noising algorithm," Opt Express, 22(26), 32119-37 (2014).
[28] J. L. Nadeau, Y. B. Cho, and C. A. Lindensmith, "Use of dyes to increase phase contrast for biological holographic microscopy," Opt Lett, 40(17), 4114-7 (2015).
[29] J. K. Wallace, S. Rider, E. Serabyn *et al.*, "Robust, compact implementation of an off-axis digital holographic microscope," Optics Express, 23(13), 17367-17378 (2015).
[30] J. Schindelin, I. Arganda-Carreras, E. Frise *et al.*, "Fiji: an open-source platform for biological-image analysis," Nat Methods, 9(7), 676-82 (2012).
[31] S. Feng, and H. G. Winful, "Physical origin of the Gouy phase shift," Opt Lett, 26(8), 485-7 (2001).
[32] L. G. Gouy, "Sur une propriété nouvelle des ondes lumineuses," CR Hebdomadaires

Séances Acad. Sci. , 110, 1251 (1890).
[33] L. Wilson, and R. Zhang, "3D Localization of weak scatterers in digital holographic microscopy using Rayleigh-Sommerfeld back-propagation," Optics Express, 20(15), 16735-16744 (2012).